

**Multi-scale computation of plant tissue  
deformation using models for individual  
cell behavior**

*Pieter Ghysels  
Giovanni Samaey  
Engelbert Tijskens  
Herman Ramon  
Dirk Roose  
Report TW 522, May 2008*



**Katholieke Universiteit Leuven**  
Department of Computer Science

Celestijnenlaan 200A – B-3001 Heverlee (Belgium)

# Multi-scale computation of plant tissue deformation using models for individual cell behavior

*Pieter Ghysels*  
*Giovanni Samaey*  
*Engelbert Tijskens*  
*Herman Ramon*

*Dirk Roose*  
*Report TW 522, May 2008*

Department of Computer Science, K.U.Leuven

## Abstract

We present a micro-macro method for the simulation of large elastic deformations of plant tissue. At the microscopic level we use a discrete element model to describe the geometrical structure and basic properties of individual plant cells. The macroscopic domain is discretized using standard finite elements, in which the unknown macroscopic material properties (the stress-strain relation) are computed using the microscopic model in small sub-domains, called *representative volume elements* (RVEs), centered around the macroscopic quadrature points. The boundary conditions for these RVEs are derived from the macroscopic deformation gradient. The computation of the macroscopic stress tensor is based on the definition of virial stress, as defined in molecular dynamics. The anisotropic Eulerian elasticity tensor is estimated using a forward finite difference approximation for the Truesdell rate of the Cauchy stress tensor. We investigate the influence of the size of the RVE and the boundary conditions via numerical experiments. We show that the multi-scale method converges to the solution of the full microscopic simulation, both for globally and adaptively refined finite element meshes and achieves a significant speed-up compared with the full microscopic simulation.

**Keywords :** multi-scale, biological tissue, RVE, virial stress.

# Multi-scale computation of plant tissue deformation using models for individual cell behavior

Pieter Ghysels    Giovanni Samaey    Engelbert Tijskens    Herman Ramon  
Dirk Roose

May 30, 2008

## Abstract

We present a micro-macro method for the simulation of large elastic deformations of plant tissue. At the microscopic level we use a discrete element model to describe the geometrical structure and basic properties of individual plant cells. The macroscopic domain is discretized using standard finite elements, in which the unknown macroscopic material properties (the stress-strain relation) are computed using the microscopic model in small sub-domains, called *representative volume elements* (RVEs), centered around the macroscopic quadrature points. The boundary conditions for these RVEs are derived from the macroscopic deformation gradient. The computation of the macroscopic stress tensor is based on the definition of virial stress, as defined in molecular dynamics. The anisotropic Eulerian elasticity tensor is estimated using a forward finite difference approximation for the Truesdell rate of the Cauchy stress tensor. We investigate the influence of the size of the RVE and the boundary conditions via numerical experiments. We show that the multi-scale method converges to the solution of the full microscopic simulation, both for globally and adaptively refined finite element meshes and achieves a significant speed-up compared with the full microscopic simulation.

## 1 Introduction

Biological materials, such as plant tissue, are inherently multi-scale in nature. One is generally interested in deformations at macroscopic length scales, which are typically much larger than the size of individual cells. At the macroscopic scale, plant tissue exhibits visco-elasto-plastic behavior, and deformation calculations for plant tissue are usually performed with the standard material laws (stress-strain relations) for visco-elasto-plastic materials, e.g. [7, 28, 32]. These models have proven their value in a wide number of engineering applications [39], but their applicability to describe mechanical deformation of plant tissue can be questioned. Moreover, such models, even if successful in describing visco-elasto-plastic deformation, do not explain *why* the underlying tissue possesses these properties. To this end, one needs to resort to more microscopic modeling techniques that take into account the structure of the tissue at the cellular level.

Several hypotheses about the visco-plastic behavior of plant tissue have been proposed in the literature. It has been suggested that visco-elastic behavior can be explained by the viscosity of the cell fluid [38] or the cell wall [23]. Alternative suggestions include the transport of air through the intracellular spaces, which can be connected through micro-channels [48]. Cell fluid can also seep through aquaporines in the cell wall, and be transported to the inter-cellular spaces or to neighboring cells, giving rise to plastic deformations [42]. Other causes of plastic behavior of the fruit tissue that have been suggested are the plasticity of the cell wall, tearing of the cell wall [21] and sliding of the cells relative to each other [20]. Up to date, there is insufficient experimental data available to be conclusive about the mechanisms at the cellular level.

So far, little work has been done to exploit information about microscopic features (at the cellular level) to construct constitutive material laws for use in continuum models; see the book by Gibson and Ashby [13] for an analytical approach to cellular solids and metal foams. At

the scale of the *individual cells*, however, one can construct more accurate (*microscopic*) models that incorporate at least some details of the interactions between individual cells, e.g. using an individual-based approach such as discrete element modeling [10]. When verified by experiments, such models can directly incorporate the visco-elasto-plastic mechanisms that are described above.

Unfortunately, simulations with such a microscopic model on macroscopic length scales are prohibitively expensive.

In this paper, we therefore propose a multi-scale method for the simulation of large elastic deformations of plant tissue. The method combines the computational efficiency of a macroscopic finite element model with the modeling accuracy of a microscopic, individual-based description. To this end, we estimate the constitutive stress-strain relation for the tissue, which is needed in the finite element model, on the fly by local simulations with a microscopic model that incorporates the effects of the cellular structure. Thus, a macroscopic analytical constitutive material law is never assumed during the computations. Whenever a stress tensor, corresponding to a given macroscopic deformation gradient, is needed in a quadrature point of the finite element mesh, a microscopic simulation is performed inside a representative volume element (RVE), centered around this quadrature point. The initial and boundary conditions for the RVE are determined by the macroscopic deformation gradient, and the corresponding stress tensor is computed from the equilibrium solution in the RVE.

For the microscopic model, we use a mass-spring method that models the cellular structure and incompressibility of cell fluid. More precisely, a two-dimensional model of a unicellular epidermis strip of onion was developed by Loodts *et al* [27]. From this model, we can compute a deformed configuration under a given load or prescribed displacement. To study the microscopic mechanics of plant tissue, a number of authors have used onion tissue because of its simple geometric structure with large cells, the lack of inter-cellular spaces and the distinct sheets that can easily be separated. We refer to work of Vanstreels *et al* [45], Hepworth and Bruce [16] and Wei *et al* [47] for the experimental determination of stress-strain curves for onion epidermis tissue using tensile tests. Blewett *et al* [3] performed compression tests on a single tomato cell to determine the elasticity of the cell wall. Since the microscopic model only describes elastic deformations correctly, we do not account for viscous and plastic effects at the macroscopic scales in the current paper.

Many authors have worked on the determination of macroscopic overall characteristics of heterogeneous materials. The most basic method for finding homogenized material properties is the *rule of mixtures*, where only the volume fractions of the microscopic constituents are taken into account. Other more advanced homogenization methods as the effective medium approximation [33, 11], the variational bounding methods [15] and mathematical asymptotic homogenization theory [2] often give reasonably good results for simple microscopic geometries and small strains. We refer to [34] for details. For the *computational* homogenization of engineering materials, micro-macro methods are described by Terada and Kikuchi [43], Smit *et al* [41], Feyel and Chaboche [12], Miehe *et al* [30, 31]. Our work is based on the approach of Kouznetsova *et al* [24, 25, 26]. Most of these methods are based on the idea of representative volume elements. With increasing computational power they have become a viable alternative to the so-called unit cell methods, which assume a specific form of the constitutive stress-strain relation, and which estimate the unknown parameters in this expression via simulations on the micro-structure, see e.g. [5, 44, 46]. Such a method, while computationally less demanding, is still limited by the assumptions made on the macroscopic constitutive relation. In the micro-macro approach, such a constitutive relation is never explicitly formulated. Instead, the stress-strain relation is evaluated from the micro-structure at the spatial point and at the time that it is required. We note that these methods are quite general, and that they can also take into account the viscous and plastic parts of the deformation, see [26] for details.

Compared to the work of Kouznetsova *et al*, in which the microscopic model inside an RVE is a finite element description of the heterogeneous material *still using a continuum description*, we use a particle-based discrete element model of the cellular structure of the plant tissue as the microscopic model. This requires us to be careful with the definition of stress. More specifically, we need to define a stress measure (based on the concept of virial stress in molecular dynamics) to enable the coupling between the microscopic discrete element model and the macroscopic

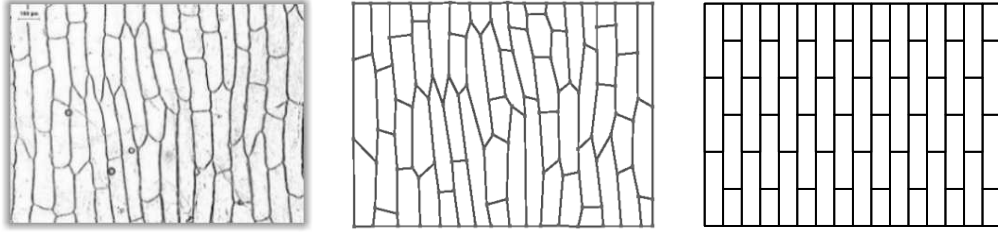


Figure 1: Left: a typical top view of a piece of onion tissue (experiment). Center: a digital version, in which every cell is modeled as a polygon. Right: a simplified version, in which the onion cells are stacked like in a brick pattern.

continuum description.

The paper is outlined as follows. In section 2.1, we describe the microscopic model for onion epidermis tissue. We give a brief overview of the large deformation continuum elasticity theory in section 2.2. Section 2.3 covers the standard finite element discretization for the elasticity equations. In section 3 we describe in detail how to combine these models into an efficient simulation. The key element in our coupling strategy is the computation of stress from an RVE at the microscopic level, given a deformation at the continuum level. The method is validated in section 4 using numerical experiments comparing the results of the coupled micro-macro simulations with the full microscopic simulation. We investigate the convergence for globally and adaptively refined meshes. In section 5, we discuss the computational efficiency and possible extensions of the method and give some references to the literature for dealing with incompressibility.

## 2 Microscopic and macroscopic models

### 2.1 The microscopic model

We start from a mechanical model of a unicellular epidermis strip of onion (*Allium cepa*), which incorporates the micro-structural behavior at the cellular level [27]. Onion was chosen because a single layer of individual cells can be isolated for experiments. Since onion cells are large and form a fairly regular structure, experimental validation of the model is feasible. Figure 1 shows how the cell structure, as seen in experiments, is simplified for use in the model.

The inherently three-dimensional onion tissue, with a constant thickness of  $120 \mu\text{m}$ , is projected on a plane, leading to a two-dimensional model, see figure 2 (left). The parts of the onion cell walls that are parallel to the plane of the epidermis strip are called the external boundaries; they form the interface between the cells and the atmosphere. The walls perpendicular to the plane of the tissue strip form the interface between the cells, and we call them internal boundaries. Every cell in the tissue is modeled as a polygon. The mass of the cell is discretized and concentrated in nodes that are placed at the corners of this polygon.

In the model the following assumptions are made: the cell wall is linearly elastic, can only resist tensile load, offers no resistance to bending, and is isotropic. Furthermore, there are no inter-cellular spaces, the cell fluid is incompressible and there is no fluid transport through cell walls. To this end, internal boundaries are modeled with internal boundary springs between the nodes along the sides of the polygons, which mimic the linear elasticity. The cell walls of neighboring cells, together with the corresponding middle lamella, are modeled as one single internal boundary spring. The external boundaries are modeled with external boundary springs.

An average onion cell is more or less rectangular with width  $480 \mu\text{m}$  and height  $120 \mu\text{m}$ . A cell is discretized with 5 nodes along its long axis and two nodes along the short axis. In the simulations the rectangular cells are ordered in a brick pattern, see figure 2 (right). For this setting, the

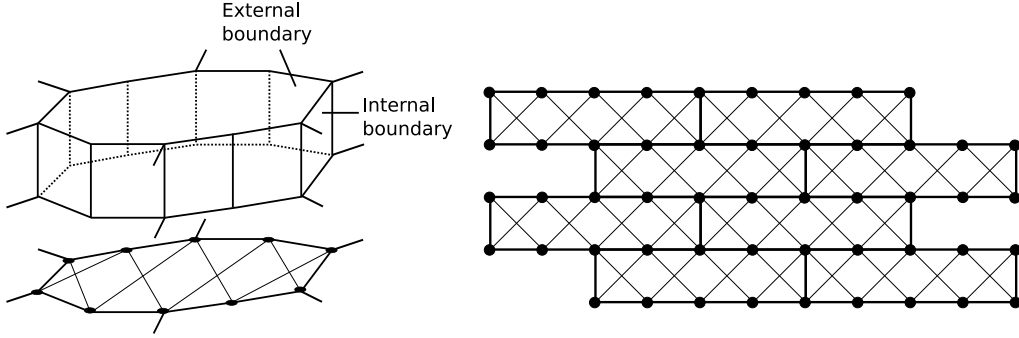


Figure 2: Left: projection of an actual three dimensional onion cell to the two-dimensional model. Cell boundaries between cells are modeled with internal boundary springs. Cell boundaries parallel to the strip of epidermis tissue are modeled with external boundary springs, diagonally in the two-dimensional cell. Right: the cells are arranged as in a brick pattern with an average aspect ratio of 1 to 4.

mass of a node can be calculated from the density of onion tissue,  $\rho = 1040 \pm 90 \text{ kg/m}^3$  to be  $m_i = 1.86 \cdot 10^{-9} \text{ kg}$ . The incompressibility of the cell fluid is approximated by means of a fictitious pressure force that penalizes the difference between the current cell volume and the desired one, i.e. the cell volume in the unloaded state  $V_k^0$ .

The dynamics of the system can be studied by time integration of the equations of motion

$$\dot{\mathbf{p}}_i = \mathbf{q}_i, \quad \dot{\mathbf{q}}_i = \frac{\mathbf{f}_i^R}{m_i} \quad (1)$$

for the nodes  $i$  with mass  $m_i$ , position  $\mathbf{p}_i$  and velocity  $\dot{\mathbf{p}}_i = \mathbf{q}_i$ . To study the deformation of a strip of onion tissue, time integration is performed until the system reaches equilibrium.

The total force  $\mathbf{f}_i^R = \mathbf{f}_i^S + \mathbf{f}_i^P + \mathbf{f}_i^E$  consists of spring forces  $\mathbf{f}_i^S$ , pressure forces  $\mathbf{f}_i^P$  and externally applied forces  $\mathbf{f}_i^E$ . The spring force  $\mathbf{f}_i^S$  in a spring connecting nodes  $i$  and  $j$  is given by

$$\mathbf{f}_{ij}^S = \begin{cases} 0 & p_{ij} \leq p_{ij}^0, \\ \left( -k_{\{I,E\}}^S (p_{ij} - p_{ij}^0) + d_{\{I,E\}}^S \dot{p}_{ij} \right) \frac{\mathbf{p}_{ij}}{p_{ij}} & p_{ij} > p_{ij}^0, \end{cases} \quad (2)$$

where  $p_{ij}^0$  is the rest length of the spring,  $\mathbf{p}_{ij} = \mathbf{p}_j - \mathbf{p}_i$  and  $p_{ij} = \|\mathbf{p}_{ij}\|$ . Based on experimental data, the spring constant was set at  $k_I^S = 1306 \text{ N/m}$  for the internal boundary springs and  $k_E^S = 1273 \text{ N/m}$  for the external boundary springs [27]. The corresponding damping constants  $d_{\{I,E\}}^S$  were chosen such that the springs are critically damped. This damping was introduced for numerical stability of the time integration of (1) and has no physical meaning. The total spring force on node  $i$  is then  $\mathbf{f}_i^S = \sum_{j \neq i} \mathbf{f}_{ij}^S$ .

The fictitious pressure force (mimicking the action of the cell fluid) on a piece of cell wall between nodes  $i$  and  $j$  is perpendicular to this wall and is evenly divided over the two nodes. For a node  $i$  the total pressure force  $\mathbf{f}_i^P$  is found by summation over the neighboring cells  $k \in C_i$  and summation over neighboring nodes  $j \in N_{ik}$  connected to node  $i$  through an internal boundary spring and belonging to cell  $k$ ,

$$\mathbf{f}_i^P = \sum_{k \in C_i} \sum_{j \in N_{ik}} - \left( k^P (V_k - V_k^0) + d^P \dot{V}_k \right) \frac{p_{ij}}{2} \mathbf{n}_{ij}, \quad (3)$$

where  $V_k$  denotes the current cell volume,  $\dot{V}_k$  its time derivative, and  $\mathbf{n}_{ij}$  is the normal direction on the piece of cell wall between nodes  $i$  and  $j$ . The cell volume  $V_k$  is computed as the surface of the polygon describing the cell and its derivative can be computed from the velocities of the

corners of the polygon  $\dot{\mathbf{p}}_i$ . We choose a large proportionality factor  $k^P = 5 \cdot 10^{10} \text{ N/m}^3$  to ensure that the regulation of the volume is achieved on a much smaller timescale than the dynamics of the system. Again, the damping constant  $d^P = 19.3 \text{ Ns/m}^3$  is chosen as to critically damp the pressure force. With these parameters, the incompressibility is approximately satisfied, with a volume change of approximately 1% for a deformation of 20%, which is sufficient for our needs. The material can be made arbitrarily incompressible by increasing the parameter  $k^P$ .

Some of the approximations in this model could be considered to be relatively crude; nevertheless, the model gives good quantitative agreement with experiments, such as those done by Wei *et al* [47].

## 2.2 Continuum elasticity theory

At the macroscopic level, the deformation of an object is described by continuum elasticity theory. In this section, we introduce the governing conservation laws, the notion of stress and its relation to deformation. The exposition will closely follow [4].

Let an object at time  $t = 0$  be defined by its space coordinates  $\mathbf{X}$  on the domain  $\kappa_0$ . The motion of this object can be described by a deformation mapping  $\mathbf{x} = \phi(\mathbf{X}, t)$  of these coordinates to the coordinates  $\mathbf{x}$  at time  $t$  in the deformed domain  $\kappa_t$ . Capital letters will refer to the initial configuration, also called the Lagrangian or material description, while lower case letters refer to the deformed state, the Eulerian or spatial description. The deformation gradient tensor is subsequently defined as

$$\mathbf{F} = \frac{\partial \phi}{\partial \mathbf{X}} = \nabla_0 \phi,$$

in which the subscript 0 denotes that the derivative is taken with respect to the original configuration. The volume change is denoted by  $J = \det \mathbf{F}$ . We define the velocity field as  $\mathbf{v}(\mathbf{x}, t) = \partial \phi(\mathbf{X}, t) / \partial t$  and the velocity field gradient is denoted by  $\mathbf{l} = \partial \mathbf{v}(\mathbf{x}, t) / \partial \mathbf{x} = \nabla \mathbf{v}$ . The symmetric part of the velocity gradient is called the rate of deformation tensor  $\mathbf{d} = (\mathbf{l} + \mathbf{l}^T) / 2$ .

Deformations introduce forces in the interior of the body, which are measured per unit area as stresses. We introduce the symmetric second order Cauchy stress tensor  $\boldsymbol{\sigma}$  which is defined in the spatial description. In the material description, we have the second Piola-Kirchhoff stress tensor  $\mathbf{S}$ , also called the engineering stress, which is related to the Cauchy stress by  $\mathbf{S} = J \mathbf{F}^{-1} \boldsymbol{\sigma} \mathbf{F}^{-T}$ . The relation between the spatial and material descriptions is given by so-called *push-forward* and *pull-back* operators  $\phi_*[\cdot]$  and  $\phi_*^{-1}[\cdot]$ , resp., that transform material quantities to their spatial analogs and vice versa. The Cauchy stress, for instance, can also be seen as a push-forward of the Piola-Kirchhoff stress,  $\phi_*[\mathbf{S}] = J \boldsymbol{\sigma}$ .

The spatial equilibrium equation is written as

$$\operatorname{div} \boldsymbol{\sigma} + \mathbf{f} = 0, \quad \text{on } \kappa_t, \quad (4)$$

where  $\mathbf{f}$  are body forces per unit volume. To obtain a closed equation, one needs a relation between the deformation  $\mathbf{F}$  and  $\boldsymbol{\sigma}$ . This relation depends on the specific material considered. For a hyperelastic material, this constitutive relation is given in the form of a strain energy function or elastic potential  $\Psi(\mathbf{F}(\mathbf{X}), \mathbf{X}) = \Psi(\mathbf{C}(\mathbf{X}), \mathbf{X})$ , which is usually written as a function of the right Cauchy-Green deformation tensor  $\mathbf{C} = \mathbf{F}^T \mathbf{F}$ . From this potential, the second Piola-Kirchhoff stress tensor can be derived as

$$\mathbf{S}(\mathbf{C}(\mathbf{X}), \mathbf{X}) = 2 \frac{\partial \Psi}{\partial \mathbf{C}}. \quad (5)$$

The time derivative of the second Piola-Kirchhoff stress tensor and the time derivative of the Cauchy-Green deformation tensor are related by the linear rate equation

$$\dot{\mathbf{S}} = \frac{1}{2} \mathbf{c} : \dot{\mathbf{C}} = \frac{1}{2} \sum_{K,L} \mathcal{C}_{IJKL} \dot{\mathbf{C}}_{KL}, \quad (6)$$

in which  $:$  denotes the double product or double contraction and the fourth order *Lagrangian elasticity tensor*  $\mathcal{C}$  is defined as

$$\mathcal{C} = 2 \frac{\partial \mathbf{S}}{\partial \mathbf{C}} = 4 \frac{\partial^2 \Psi}{\partial \mathbf{C} \partial \mathbf{C}}.$$

Note that  $\mathcal{C}_{IJKL} = \mathcal{C}_{KLIJ}$ .

Equation (6) can also be written in the spatial description by performing a push-forward operation on  $\dot{\mathbf{C}}$  and  $\dot{\mathbf{S}}$  [4]. The push-forward of  $\dot{\mathbf{C}}/2$  is the rate of deformation tensor  $\mathbf{d}$ . The push-forward of  $\dot{\mathbf{S}}$  is the Truesdell rate of the Cauchy stress tensor, defined as

$$\boldsymbol{\sigma}^\circ = J^{-1} \mathcal{L}_\phi[J\boldsymbol{\sigma}] = \dot{\boldsymbol{\sigma}} - \mathbf{l}\boldsymbol{\sigma} - \boldsymbol{\sigma}\mathbf{l}^T + (\text{tr}\mathbf{l})\boldsymbol{\sigma}.$$

Here  $\mathcal{L}_\phi[\cdot] = \phi_*[\text{d}/\text{dt}(\phi_*^{-1}[\cdot])]$  denotes the Lie type derivative, which is defined as the push-forward of the time derivative of the pull-back. The spatial analog of the Lagrangian elasticity tensor is the fourth order *spatial Eulerian elasticity tensor*  $\mathbf{c}$ , which is related to the Lagrangian elasticity tensor via

$$c_{ijkl} = J^{-1} F_{iI} F_{jJ} F_{kK} F_{lL} \mathcal{C}_{IJKL} = c_{klij}.$$

The spatial analog of (6) then becomes

$$\boldsymbol{\sigma}^\circ = \mathbf{c} : \mathbf{d}. \quad (7)$$

For the plant tissue considered in this work, the elastic potential  $\Psi(\mathbf{C}(\mathbf{X}), \mathbf{X})$  is not explicitly available. Instead, the relations (5) and (6) have to be estimated via a simulation with the microscopic model described in section 2.1.

### 2.3 Finite element formulation

In this section, we briefly describe the finite element discretization. We have chosen to use an updated Lagrangian formulation, but an equivalent total Lagrangian formulation is also conceivable [26], and would not influence the multi-scale coupling strategy of the present paper. Because the microscopic model allows small volume changes (of approximately one percent for large deformations), no special precaution is necessary here to avoid the phenomenon of *volumetric locking* that is common in finite element simulations of incompressible materials [4].

Multiplying equation (4) with a test function  $\delta\mathbf{v}$  and integrating over the domain  $\kappa_t$  gives the spatial virtual work equation

$$\int_{\partial\kappa_t} \mathbf{n} \cdot \boldsymbol{\sigma} \delta\mathbf{v} da - \int_{\kappa_t} \boldsymbol{\sigma} : \nabla \delta\mathbf{v} dv + \int_{\kappa_t} \mathbf{f} \cdot \delta\mathbf{v} dv = 0, \quad (8)$$

with  $\mathbf{n}$  the normal vector on the boundary  $\partial\kappa_t$ . This equation naturally leads to a displacement finite element method. For notational convenience, we omit (for now) the traction  $\mathbf{n} \cdot \boldsymbol{\sigma}$  on the boundary  $\partial\kappa_t$ . We approximate the domain  $\kappa$  by a set of  $n_{el}$  finite elements  $\kappa_e$ , in which the continuum displacement field  $\mathbf{u} = \mathbf{x} - \mathbf{X}$  is discretized as  $\tilde{\mathbf{u}} = \tilde{\mathbf{x}} - \tilde{\mathbf{X}}$ . Here, the tilde indicates that the quantities are only defined at discrete nodal points. The displacements of other points can be found by linear interpolation  $\mathbf{u} \approx \sum_a N_a \tilde{\mathbf{u}}_a$  where  $N_a$  is the shape function corresponding to node  $a$ . Discretization of (8) leads to a nonlinear system of equations, in which the unknowns  $\tilde{\mathbf{u}}$  are the nodal displacements in each coordinate direction and for every node  $a$

$$\sum_e^{n_{el}} \left( \int_{\kappa_e} \boldsymbol{\sigma}(\tilde{\mathbf{u}}) \nabla N_a dv - \int_{\kappa_e} \nabla N_a \mathbf{f} dv \right) = 0, \quad \forall a. \quad (9)$$

In each step of a Newton-Raphson method, equation (9) is linearized,

$$\sum_e^{n_{el}} \left( \left( \int_{\kappa_e} \nabla N_a \cdot \boldsymbol{\sigma} \nabla N_b dv \right) \mathbf{I} + \int_{\kappa_e} \mathbf{B}_a^T \mathbf{D} \mathbf{B}_b dv \right) \Delta \tilde{\mathbf{u}} = - \sum_e^{n_{el}} \left( \int_{\kappa_e} \boldsymbol{\sigma} \nabla N_a dv - \int_{\kappa_e} \nabla N_a \mathbf{f} dv \right), \quad (10)$$

where in the case of plane strain,

$$\mathbf{D} = \frac{1}{2} \begin{bmatrix} 2c_{1111} & 2c_{1122} & c_{1112} + c_{1121} \\ & 2c_{2222} & c_{2212} + c_{2221} \\ \text{sym} & & c_{1212} + c_{1221} \end{bmatrix}, \quad (11)$$

denotes the spatial constitutive matrix and  $\mathbf{B}_a$  the strain-displacement matrix,

$$\mathbf{B}_a^T = \begin{bmatrix} \partial N_a / \partial x & 0 & \partial N_a / \partial y \\ 0 & \partial N_a / \partial y & \partial N_a / \partial x \end{bmatrix}.$$

The vector of unknowns  $\Delta \tilde{\mathbf{u}}$  gives a correction to the discrete displacements  $\tilde{\mathbf{u}}$  of the nodal points. The right hand side of (10) is the residual of the discretized virtual work theorem

$$\mathbf{R}_a = \sum_e^{n_{el}} \left( \int_{\kappa_e} \boldsymbol{\sigma} \nabla N_a dv - \int_{\kappa_e} \nabla N_a \mathbf{f} dv \right). \quad (12)$$

We introduce the assembled tangent stiffness matrix  $\mathbf{K}$ , whose elements are

$$\mathbf{K}_{ab} = \sum_e^{n_{el}} \left( \mathbf{K}_{\boldsymbol{\sigma}, ab}^{(e)} + \mathbf{K}_{\mathbf{c}, ab}^{(e)} \right).$$

Here,  $\mathbf{K}_{\boldsymbol{\sigma}, ab}^{(e)}$  is the initial stress component,

$$\mathbf{K}_{\boldsymbol{\sigma}, ab}^{(e)} = \left( \int_{\kappa_e} \nabla N_a \cdot \boldsymbol{\sigma} \nabla N_b dv \right) \mathbf{I}, \quad (13)$$

and  $\mathbf{K}_{\mathbf{c}, ab}^{(e)}$  the constitutive component of the tangent matrix,

$$\mathbf{K}_{\mathbf{c}, ab}^{(e)} = \int_{\kappa_e} \mathbf{B}_a^T \mathbf{D} \mathbf{B}_b dv. \quad (14)$$

Equation (10) can then be written in short as

$$\mathbf{K} \Delta \tilde{\mathbf{u}} = -\mathbf{R}. \quad (15)$$

To solve equation (15), we need to evaluate the integrals in the expressions for the stiffness matrix ((13) and (14)) and the right hand side (12) of the linear equation. To this end, we use a numerical quadrature rule. One then only needs the value of the Cauchy stress and the spatial elasticity tensor  $\mathbf{c}$  in the quadrature points; since we do not have a closed macroscopic model, this information will be estimated using the microscopic model described in section 2.1.

Note that the inclusion of traction on the boundary would lead to an additional term in the total assembled stiffness matrix, which does not depend on the material parameters.

### 3 Computation of macroscopic quantities

The macroscopic domain is discretized with a (macroscopic) finite element mesh. This discretization is coupled to microscopic simulations in small subdomains centered around each macroscopic quadrature point (so-called *representative volume elements*, or RVEs). This micro-macro method is also called the RVE method [24]. The goal of these RVEs is to replace the constitutive relation, which is assumed to exist but is unavailable in closed form.

In each quadrature point, the Cauchy stress  $\boldsymbol{\sigma}$  and the spatial elasticity tensor  $\mathbf{c}$  need to be estimated from the RVE. To this end, micro-structural simulations are performed using boundary conditions derived from the macroscopic displacement field. We compute the steady state solution of the RVE in the absence of external forces, i.e. the displacements on the RVE that satisfy

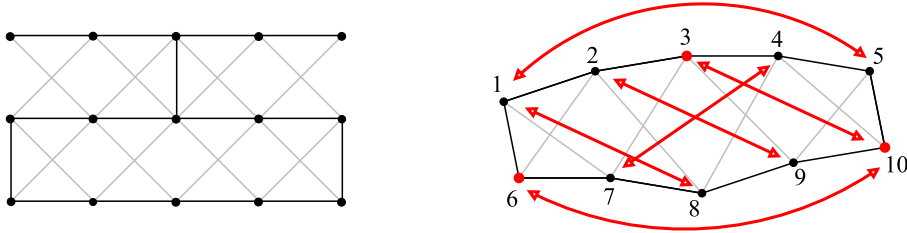


Figure 3: Left: one period of the brick pattern. Right: in the implementation only one cell is used with shifted periodic boundary conditions. Nodes 1-6 correspond with nodes 5-10 in the horizontal direction. Nodes 3-4-5 correspond with nodes 6-7-8 and nodes 1-2-3 with 8-9-10 in the vertical direction. This way the brick pattern is preserved by simulating only one cell.

$\text{div } \boldsymbol{\sigma} = 0$  on  $V^{\text{RVE}}$ . External forces can be included afterwards at the macroscopic level in the finite element model. The required stress at the quadrature point is then simply the volume average of the stress tensor in the RVE; the corresponding elasticity tensor can be approximated using a forward difference technique.

Two aspects are important when implementing the RVE method. In general, the size of the RVE should be of the order of the characteristic length of the micro-structure of the material; when this length scale is much smaller than the macroscopic domain under consideration, the method achieves a good speedup compared to the full microscopic simulation. Second, it is important to choose the boundary conditions of the RVE carefully to avoid bias in the stress estimates.

In the next subsections, we will give a detailed description of the implementation of the RVE method: we will show how we choose the RVE and apply boundary conditions (section 3.1), how to compute the Cauchy stress (section 3.2), and the spatial elasticity tensor (section 3.3).

### 3.1 Applying deformation on the RVE

To compute the stress corresponding to a given deformation in each RVE, we first impose the required deformation via appropriate boundary conditions (BCs), after which we compute the steady state solution. In principle, periodic, Dirichlet or Neumann boundary conditions may be applied; however, it is shown in [43], that periodic boundary conditions are often the best choice.

In this case, we use periodic boundary conditions. It can easily be seen that the micro-structure in this model in the undeformed, idealized state, is periodic with one period given by figure 3 (left). However, by a careful implementation of the boundary conditions, simulations can also be performed using an RVE consisting of only one onion cell.

As was also shown in [29], the deformation can be applied by imposing the displacement on three points and holding these points fixed during the simulation. Displacements  $\tilde{\mathbf{u}}_6$ ,  $\tilde{\mathbf{u}}_3$  and  $\tilde{\mathbf{u}}_{10}$  for the nodes 6, 3 and 10, see figure 3 (right), are computed from the macroscopic deformation gradient as

$$[\tilde{\mathbf{u}}_6 \quad \tilde{\mathbf{u}}_3 \quad \tilde{\mathbf{u}}_{10}] = [\mathbf{F}_M - \mathbf{I}] \cdot [\mathbf{X}_6 \quad \mathbf{X}_3 \quad \mathbf{X}_{10}],$$

with  $\mathbf{F}_M$  the deformation gradient at the quadrature point as computed by the macroscopic finite element model and  $\mathbf{X}_i$  the initial position of node  $i$ . Periodicity is enforced by letting forces, acting from the interior of the cell on a node on the boundary of the domain, act on the corresponding node of the opposite wall as well, see figure 3 (right). For consistency we need  $\mathbf{F}_M = \bar{\mathbf{F}}_\mu$ , the macroscopic deformation gradient  $\mathbf{F}_M$  must be equal to the volume average of the microscopic deformation gradient over the RVE,  $\bar{\mathbf{F}}_\mu$ ,

$$\bar{\mathbf{F}}_\mu = \frac{1}{V_0^{\text{RVE}}} \int_{V_0^{\text{RVE}}} \mathbf{F}_\mu dV_0,$$

in which the integral is taken over the initial volume of the RVE since the deformation gradient

is defined over the initial configuration. In appendix A, this is shown for the combination of boundary conditions and prescribed displacements that were used here.

### 3.2 Computation of stresses

Once the deformation is applied, the equations of motion for the nodes (1) are integrated in time until equilibrium is reached. Subsequently, the average stress in the RVE is computed.

Since the notion of stress finds its origin in the classical continuum theory, we need to take care in defining an appropriate measure for stress on the microscopic (discrete) level. Here, we use the *virial stress*, based on Clausius' virial theorem, which is often used in molecular dynamics and other particle system simulations [9, 49, 37]. The average virial (or Irving-Kirkwood [19]) stress over a volume  $\Omega$  is defined as

$$\boldsymbol{\sigma}^v = \frac{1}{\Omega} \sum_{i \in \Omega} \left( -m_i (\dot{\mathbf{p}}_i - \bar{\dot{\mathbf{p}}}) \otimes (\dot{\mathbf{p}}_i - \bar{\dot{\mathbf{p}}}) + \frac{1}{2} \sum_{j \in \Omega} \mathbf{f}_{ij} \otimes (\mathbf{p}_j - \mathbf{p}_i) \right),$$

with  $m_i$  the mass of node  $i$ ,  $\mathbf{p}_i$  its position,  $\dot{\mathbf{p}}_i$  its velocity,  $\bar{\dot{\mathbf{p}}}$  the average particle velocity and  $\mathbf{f}_{ij}$  the force between particles  $i$  and  $j$ . The symbol  $\otimes$  denotes a dyadic or tensor product of two vectors. There is some discussion in the literature on how the first term, which corresponds to a mass transfer in the volume, should be interpreted, see e.g. the discussions in the work of Zhou [49] and Chen and Fish [8] and references therein. In the equilibrium state we are interested in, this term is zero.

The second term, corresponding to the forces between the nodes, is analogous to the interpretation of mechanical stress in the continuum theory. In this formula, we include all forces that arise from the springs that directly connect two masses; we call the corresponding stress tensor the “spring stress tensor”, and it is given as

$$\bar{\boldsymbol{\sigma}}^s = \frac{1}{2V^{\text{RVE}}} \sum_{i,j \in \text{RVE}} \mathbf{f}_{ij}^S \otimes (\mathbf{p}_j - \mathbf{p}_i). \quad (16)$$

The resulting tensor will always be symmetric since each spring force is parallel to the line connecting the two points.

If in equation (16) the original nodal positions  $\mathbf{p}_i^0$  and the original volume  $V_0^{\text{RVE}}$  are used instead of the current ones, the corresponding stress would be the first Piola-Kirchhoff stress tensor  $\bar{\mathbf{P}}$ .

This definition of the stress so far does not include the hydrostatic stress in the cell fluid. (It only contains components arising from the springs directly connecting two masses.) Since the hydrostatic stress is isotropic, it can be captured by a scalar quantity, the pressure  $p$ . This additional stress component can be added to the spring stress tensor as

$$\bar{\boldsymbol{\sigma}}^{\text{RVE}} = \bar{\boldsymbol{\sigma}}^s + p\mathbf{I}.$$

The pressure in a cell is proportional to the difference in current cell volume  $V_k^t$  and desired cell volume  $V_k^0$  with a proportionality factor  $k^P$  as in section 2.1. The RVE pressure is the average over the different cells in the RVE

$$p = -\frac{1}{n_c} \sum_{k \in \text{RVE}} k^P (V_k^t - V_k^0) \quad (17)$$

with  $n_c$  the number of cells in the RVE.

The tensor  $\bar{\boldsymbol{\sigma}}^{\text{RVE}}$  can be used in the finite element code as the macroscopic stress tensor at the corresponding quadrature point. It can be checked that it is an objective stress measure, i.e. the stress tensor of an RVE transformed by a rigid body motion  $\mathbf{Q}$  satisfies  $\bar{\boldsymbol{\sigma}} = \mathbf{Q}\bar{\boldsymbol{\sigma}}^{\text{RVE}}\mathbf{Q}^T$ .

### 3.3 Spatial elasticity tensor

To compute the spatial elasticity tensor, we follow the general approach proposed by Miehe [30], which is based on a forward finite difference approximation and requires only the calculation of stress tensors for slightly perturbed deformation gradients. Using this procedure, the microscopic simulator only needs to compute a stress tensor for a given deformation gradient. We note that if, additionally, a microscopic Jacobian matrix would be available, the elasticity tensor can be found by a condensation of this matrix [24].

We start by approximating the time derivative of the Cauchy stress with a forward finite difference formula as

$$\begin{aligned}\dot{\boldsymbol{\sigma}} &= \frac{d\boldsymbol{\sigma}(\mathbf{F}(\mathbf{X}, t))}{dt} \\ &\approx \frac{\boldsymbol{\sigma}(\mathbf{F}(\mathbf{X}, t + \epsilon)) - \boldsymbol{\sigma}(\mathbf{F}(\mathbf{X}, t))}{\epsilon} \\ &\approx \frac{\boldsymbol{\sigma}(\mathbf{F}(\mathbf{X}, t) + \epsilon \dot{\mathbf{F}}(\mathbf{X}, t)) - \boldsymbol{\sigma}(\mathbf{F}(\mathbf{X}, t))}{\epsilon} \\ &= \frac{\boldsymbol{\sigma}(\mathbf{F} + \epsilon \dot{\mathbf{F}}) - \boldsymbol{\sigma}(\mathbf{F})}{\epsilon},\end{aligned}$$

where  $\epsilon$  is a small perturbation parameter. If we replace the linearized deformation gradient  $\dot{\mathbf{F}}$  by the elementary deformation tensor in the indices  $(kl)$

$$\dot{\mathbf{F}}^{(kl)} = \mathbf{e}_k \otimes (\mathbf{e}_l \mathbf{F})$$

with  $\mathbf{e}_k$  the unit vector and use the fact that the velocity gradient  $\mathbf{l} = \dot{\mathbf{F}}\mathbf{F}^{-1}$ , we have

$$\mathbf{l}^{(kl)} = \dot{\mathbf{F}}^{(kl)} \mathbf{F}^{-1}.$$

Inserting the approximation for  $\dot{\boldsymbol{\sigma}}$  in the linearized constitutive relation (7) gives

$$\frac{\boldsymbol{\sigma}(\mathbf{F} + \epsilon \dot{\mathbf{F}}^{(kl)}) - \boldsymbol{\sigma}}{\epsilon} - \mathbf{l}^{(kl)} \boldsymbol{\sigma} - \boldsymbol{\sigma} \mathbf{l}^{(kl)T} + \text{tr}(\mathbf{l}^{(kl)}) \boldsymbol{\sigma} = \mathbf{c} : \frac{\mathbf{l}^{(kl)} + \mathbf{l}^{(kl)T}}{2},$$

from which a relation for the elements of the symmetrized Eulerian elasticity tensor  $\mathbf{c}$

$$\frac{\mathbf{c}_{ij(kl)} + \mathbf{c}_{ij(lk)}}{2} = \left[ \frac{\boldsymbol{\sigma}(\mathbf{F} + \epsilon \dot{\mathbf{F}}^{(kl)}) - \boldsymbol{\sigma}}{\epsilon} - \mathbf{l}^{(kl)} \boldsymbol{\sigma} - \boldsymbol{\sigma} \mathbf{l}^{(kl)T} + \text{tr}(\mathbf{l}^{(kl)}) \boldsymbol{\sigma} \right]_{ij}, \quad (18)$$

can be derived. Performing these calculations for combinations of  $k$  and  $l$  gives the values which are needed to construct the constitutive matrix  $\mathbf{D}$  from equation (11). For plane strain, only three extra stress calculations have to be performed.

In our simulations, we will set the perturbation parameter  $\epsilon = \sqrt{\epsilon_{\text{mach}}} = 10^{-8}$ , in which  $\epsilon_{\text{mach}} \approx 10^{-16}$  is the machine precision for double precision floating point calculations [22].

## 4 Numerical results

In this section, we illustrate the behavior of the RVE method. In section 4.1, we show the convergence of the computed stress in one RVE. Sections 4.2 and 4.3 contain numerical convergence tests for a uniaxial and arbitrary deformation, resp.

### 4.1 Computation of stresses

After applying an initial deformation to the RVE, time integration of the equations of motion for the nodes (1) of the micromodel for a sufficiently long time leads to the steady state of the RVE.

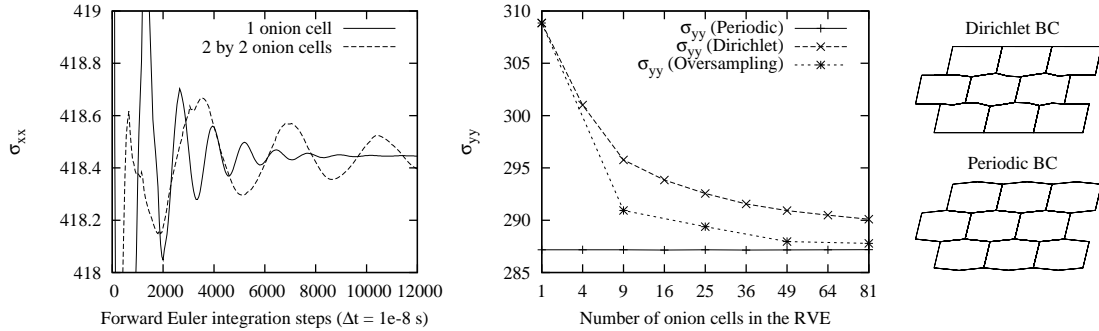


Figure 4: Left: the time-evolution of the  $\sigma_{xx}$  component of the average Cauchy stress in the RVE for 2 different sizes of the RVE, a single onion cell (solid line) and 4 (2 by 2) onion cells (dashed line). The smaller RVE converges in significantly less time steps. Center:  $\sigma_{yy}$  of the RVE in equilibrium with periodic and Dirichlet boundary conditions for varying number of onion cells in the RVE. Right, top: an RVE with 9 onion cells deformed with Dirichlet BC's. Right, bottom: the same RVE deformed with periodic BC's. Here the boundary is free to deform.

For this integration, we use a forward Euler method with a time step  $\Delta t = 10^{-8}$  s, which was implemented in a code developed by Loodts [27].

Figure 4 (left) shows the evolution of  $\sigma_{xx}$  as a function of time for an RVE with 1 onion cell and for an RVE with 4 (2 by 2) onion cells using the boundary conditions described in section 3.1. The three fixed nodes are moved by the deformation gradient

$$\mathbf{F} = \begin{bmatrix} 1 & 0.5 \\ 0 & 1 \end{bmatrix} \quad (19)$$

which represents a pure shear with an angle of 30 degrees. We see from figure 4 (left) that an RVE with more cells requires considerably more time steps to converge to equilibrium.

Different choices of boundary conditions (such as Dirichlet) can lead to a biased boundary layer [14], a problem which can be overcome by oversampling, i.e. using only a subdomain of the RVE in the volume averaging of the computation of the macroscopic quantities. Figure 4 (right) shows two RVEs with 9 onion cells deformed with the deformation gradient given in (19), one with Dirichlet boundary conditions (top) and the other with periodic boundary conditions (bottom). We compare the computed stresses from RVEs with periodic with Dirichlet boundary conditions (with and without oversampling) for increasing RVE size. In the oversampling case, the volume average is always computed over one onion cell (the middle one). Figure 4 (center) shows the results. We see that for periodic boundary conditions, the stress at equilibrium does not depend on the size of the RVE. With Dirichlet BC there are more constraints on the boundary, which leads to larger stress values; however, with increasing RVE size, we observe convergence towards the stress that was computed with periodic BC. With oversampling, the error with respect to the periodic case is systematically smaller.

To decide when the time integration in the RVE has reached steady state, we proceed as follows. The averaged stress tensor in the RVE is computed every 10 time steps, and the RVE is assumed to be in equilibrium when the relative or absolute difference between the Frobenius norm of two consecutive stress tensors is smaller than  $10^{-12}$  thus when

$$\min \left( \frac{\|\boldsymbol{\sigma}^i - \boldsymbol{\sigma}^{i+10\Delta t}\|_F}{\|\boldsymbol{\sigma}^i\|_F}, \|\boldsymbol{\sigma}^i - \boldsymbol{\sigma}^{i+10\Delta t}\|_F \right) < 10^{-12}, \quad \|\boldsymbol{\sigma}\|_F^2 = \sum_{i=1}^2 \sum_{j=1}^2 |\sigma_{ij}|^2.$$

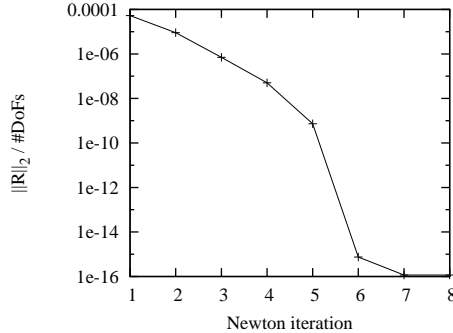


Figure 5: For a regular grid as shown in figure 6 (left) Newton’s method to solve the nonlinear FE equation converges quadratically to machine precision.

## 4.2 Equilibrium computation for uniaxial deformation

We proceed with the computation of the deformation of a square piece of onion tissue of 12 mm by 12 mm. The deformation is simulated with the coupled micro-macro solver and compared with the reference solution, obtained with the microscopic model on the whole domain. The strip consists of 25 by 100 onion cells, ordered in a brick pattern. The left boundary of the domain is held fixed and on the right boundary a displacement is prescribed so that the strip is stretched 20% along the x axis, which was chosen to show that the multi-scale approach stays valid even for geometrically nonlinear deformations. We have to note, however, that this deformation is beyond the validated range of the microscopic model.

### 4.2.1 Convergence

We computed a reference solution with the full microscopic model. Note that the 20% deformation could not be imposed at once for numerical stability reasons and we needed to apply the deformation in 100 incremental steps. The system is assumed to be in steady state if

$$\frac{\sum_{i=1}^N \|\dot{\mathbf{p}}_i\|_2}{N} < 10^{-12},$$

with  $\dot{\mathbf{p}}_i$  the velocity of node  $i$  and  $N$  the total number of nodes in the system.

The finite element model was implemented using the general purpose finite element library deal.ii [1]. The 12 by 12 mm domain was discretized with 32 by 32 square bilinear Lagrange finite elements and stretched by 20% along the x axis. Integration over the elements is done with a Gauss formula with 4 quadrature points per element. The RVE consists of 1 onion cell with periodic boundary conditions. The nonlinear finite element equation is solved with a Newton’s method, in which a linear system is solved in each step with CG preconditioned with SSOR with relaxation parameter  $\omega = 1.2$ . The error of the Newton process was defined as the  $L_2$  norm of the residual vector divided by the number of degrees of freedom. Figure 5 shows the quadratic convergence of this error as a function of the number of Newton iterations to machine precision. Figure 6 shows that there is a good agreement between the deformed domain computed with the coupled micro-macro approach and the full microscopic solution.

### 4.2.2 Finite size effects

When the finite elements get larger with respect to the onion cells, there is a larger separation between the microscopic and macroscopic spatial scales. Since an onion cell has a fixed size, we varied the size of *the domain* with fixed number of elements instead to investigate the influence of

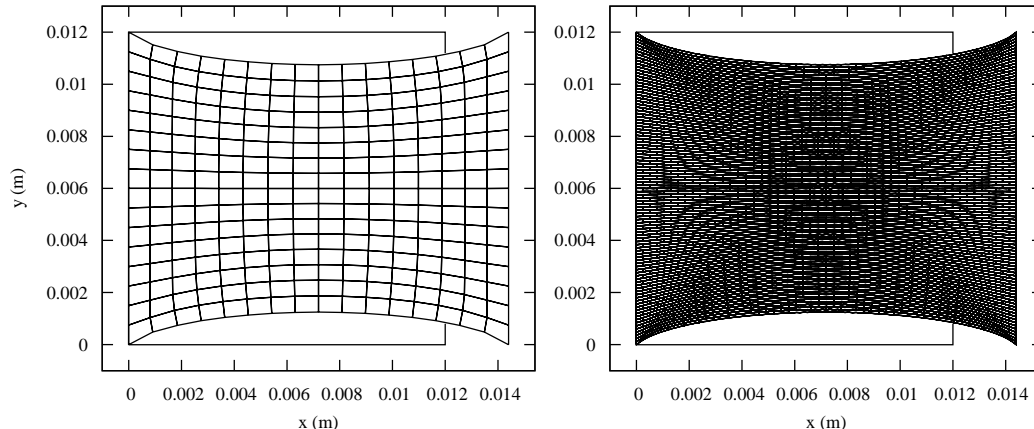


Figure 6: The deformed onion strip of 12 mm by 12 mm as computed with the coupled micro-macro model (left) and the full microscopic model (right). The domain is discretized with 16 by 16 bilinear finite elements. The microscopic domain consists of 25 by 100 onion cells.

the separation in scales. The microscopic domain was again stretched 20% along the x axis. We started from an initial finite element mesh with 2 by 2 elements that are refined successively.

The error of the coupled micro-macro simulation is defined as the deviation from the reference solution and it is measured by

$$e = \frac{\max \|\mathbf{p}_i^\mu - \mathbf{p}_i^M\|_2}{L} \quad (20)$$

with  $L$  the size of the domain,  $\mathbf{p}_i^\mu$  the current position of the microscopic node  $i$  and  $\mathbf{p}_i^M$  the deformed coordinates of the point corresponding to the initial position of node  $i$  computed by evaluating the finite element solution.

Figure 7 (left) shows the error, as defined in equation (20) as a function of the inverse mesh size  $h^{-1}$  for different domain sizes. We see that the error levels off when the finite element mesh size becomes smaller than the typical size of the onion cells, i.e.  $h = \sqrt{120\mu\text{m} \cdot 480\mu\text{m}} = 240\mu\text{m}$  denoted by the vertical line. (For larger domains the error levels off before reaching the microscopic accuracy because of numerical errors due to finite differencing, i.e. by only approximately computing the stress tensor at each quadrature point and in approximating the spatial elasticity tensor  $\mathbf{c}$  using the forward difference formula (18)). The convergence rate is approximately second order in  $h$ , thus  $e = \mathcal{O}(h^2)$  which is to be expected for bilinear finite elements.

Figure 7 (right) shows the same error but as a function of the total number of degrees of freedom in the finite element simulation. It can be seen that for meshes that are coarse compared to the microscopic scale, the error is independent of the size of the RVE. Only when the total number of degrees of freedom in the FEM exceeds the number of variables in the microscopic simulation, the error levels off. For larger domains or RVEs smaller relative to the domain size, the macroscopic model can be refined further which leads to smaller minimal errors.

### 4.3 Arbitrary deformation

To demonstrate the method also works on more arbitrary cases of deformation the same original domain as before (12 by 12 mm) is initially deformed as

$$(x, y) = \phi(X, Y) = (0.2X + 4YX/0.012, -0.1X)$$

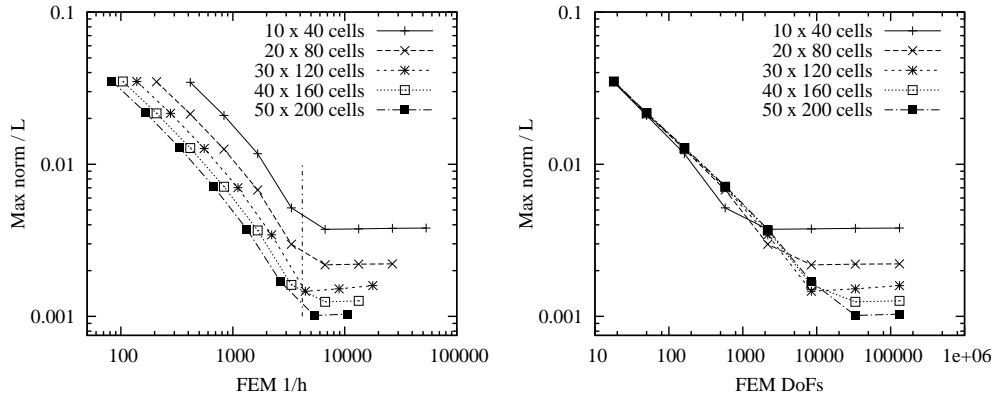


Figure 7: The  $L_\infty$  norm (max norm) of the difference between microscopic and coupled micro-macro model solutions for successively finer meshes and for different domains. Left: error as a function of the inverse of the finite element mesh size. Right: error as a function of the total number of degrees of freedom in the finite element simulation.

and the left ( $X = 0$ ) and right ( $X = 0.012$ ) edges of the domain are held fixed. Figure 8 (left) shows the system in equilibrium as computed with the coupled micro-macro approach. Here an adaptive finite element method was used based on an error estimator by Kelly, Gago, Zienkiewicz and Babuska [50], which is available in the deal.ii library [1]. Only 30% of the elements with the largest error are refined. Figure 8 (right) shows the same problem computed with the full microscopic simulator.

## 5 Discussion

### 5.1 Computational efficiency

The total computational cost of the micro-macro coupled approach is proportional to the number of simulated onion cells times the total simulated time per onion cell.

#### 5.1.1 Number of microscopic simulations

Let  $q$  be the total number of quadrature points on the finite element domain. Evaluating the residual vector requires  $q$  microscopic simulations, one in every quadrature point. Assembling the stiffness matrix requires three extra microscopic simulations per quadrature point to estimate the spatial elasticity tensor  $\mathbf{c}$ . Thus assembling the linear system takes  $4q$  microscopic simulations, which leads to a total of  $4qm$  calls to the micro model, with  $m$  the number of Newton iterations. The coupled micro-macro simulation depicted in Figure 6 required in total 28672 microscopic simulations ( $16^2$  elements, 4 quadrature points per element, 4 simulations for estimating the elasticity tensor and 7 Newton iterations).

We note that when using an iterative Krylov method, such as GMRES or CG, we could also choose to compute each matrix-vector product as

$$\mathbf{K}(\tilde{\mathbf{x}}) \Delta \tilde{\mathbf{u}} \approx \frac{\mathbf{R}(\tilde{\mathbf{x}} + \epsilon \Delta \tilde{\mathbf{u}}) - \mathbf{R}(\tilde{\mathbf{x}})}{\epsilon}, \quad (21)$$

with  $\epsilon$  a properly chosen perturbation parameter, see [6, 36], and never assemble the complete stiffness matrix  $\mathbf{K}$ . However, we can easily see that this approach will require more microscopic simulations, since using equation (21) requires  $q(n+1)$  microscopic simulations, with  $n$  the number of Krylov iterations, whereas a direct assemble only requires  $4q$  microscopic simulations.

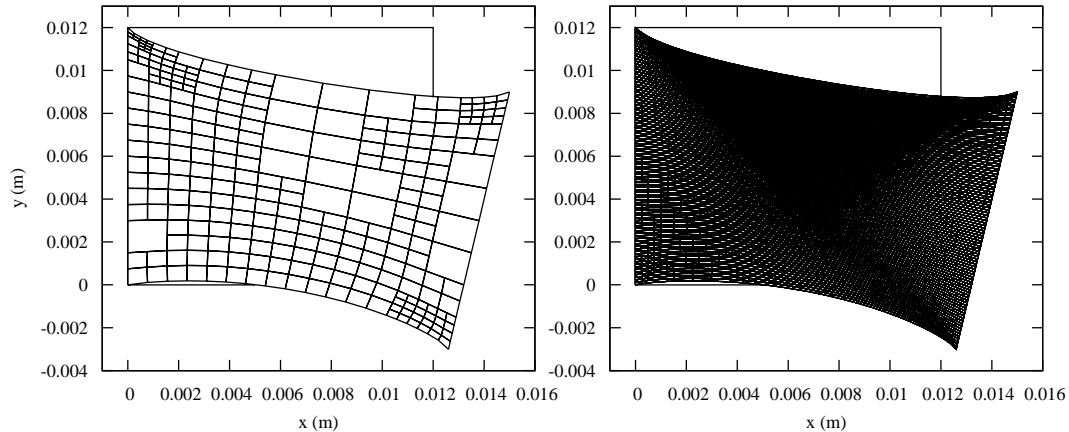


Figure 8: An arbitrary deformation. Left: The coupled micro-macro simulation with adaptive mesh refinement. Right: The full microscopic simulation.

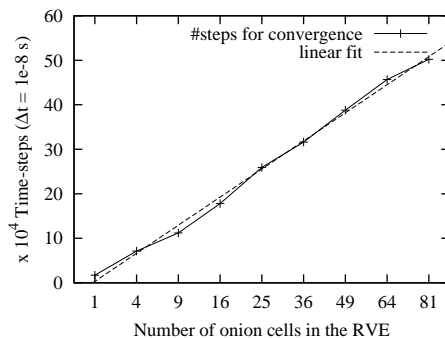


Figure 9: Required number of time-steps to reach the steady state of the RVE as a function of number of onion cells.

The number of microscopic simulations can be reduced by reducing the number of Newton iterations. This can be achieved when an approximate analytical constitutive model for the material is known, since this model can be used to find a good initial guess for the Newton process. Computing this initial guess is computationally cheap compared to the coupled micro-macro simulations. When a good initial solution is found, the Newton method will quickly reach its zone of quadratic convergence and then only a few iterations with the full coupled system are necessary to converge to machine precision. Alternatively, one could keep the stiffness matrix fixed during some Newton iterations (a quasi Newton method).

### 5.1.2 Simulation time per onion cell

Figure 9 shows the required number of time-steps to reach the steady state of the RVE as a function of number of onion cells. From this figure we can observe that the required number of times-steps to reach the equilibrium increases drastically for growing domains. For an RVE with a single onion cell, on average 17020 time-steps are needed to reach the steady state of the RVE.

The total cost of the coupled micro-macro simulation can be estimated as 17020 time-steps per onion cell times 28672 simulated onion cells, which totals  $4.8 \cdot 10^8$ .

Extrapolating the data from figure 9 to the 2500 onion cells that were used in the full microscopic simulation, we could expect the total number of time-steps required in the full simulation to be approximately  $3.2 \cdot 10^6$ . Applying the macroscopic deformation in 100 incremental steps reduced this number somewhat to  $1.04 \cdot 10^6$ . Multiplying this with the total number of simulated onion cells yields an estimate for the total cost of the full microscopic simulation of  $2.6 \cdot 10^9$ .

So, since the overhead of solving the linear equations (15) is negligible, a speedup with a factor 5 can be achieved, which is in line with our wall clock timings.

We emphasize that this speedup is achieved even with more simulated onion cells in the coupled micro-macro simulation than in the full microscopic simulation, due to the fact that the necessary simulation time to reach equilibrium increases as a function of the number of *coupled* onion cells. With a larger separation between microscopic and macroscopic scales, larger speedups are to be expected. Also, for larger domains, the number of onion cells inevitably has to increase, since an onion cell has a fixed size; hence the computational cost of a full microscopic simulation grows rapidly with the size of the domain. On the other hand, the micro-macro approach scales with the number of finite elements that are needed to accurately represent the deformation; this number can be independent of the physical size of the domain.

## 5.2 Incompressibility

As was discussed in section 2.1, the incompressibility of the onion tissue was only approximately modeled, leading to small volume changes of the order of one percent for large deformations for our choice of parameters. With these parameters, the standard displacement-based finite element method, as described above, is sufficient. However when the parameters are chosen such that the material becomes more incompressible, the performance of the standard displacement based finite element method will rapidly decrease, due to *volumetric locking* [4, 50]. Special finite element techniques have been developed to cope with these problems, ranging from reduced or selective reduced integration [18] and the B-bar method [17] to sophisticated techniques such as the *enhanced assumed strain* (EAS) method [40].

Some methods are based on a mixed displacement-pressure (u-p) functional [51], and can readily be applied in our multi-scale context. To this end, one needs to split the deformation in a deviatoric and a volumetric component. Only the deviatoric part is applied as a deformation on the RVE; the volumetric part is treated separately using a penalizing pressure term. For nearly incompressible materials, such as the onion tissue considered here, the bulk modulus needs to be known; this parameter depends on the parameters of the microscopic model (in particular the volume constraint) in a non-trivial manner.

## 6 Conclusions and outlook

We presented a micro-macro approach, based on the concept of representative volume elements (RVEs) to the computation of large elastic deformations of plant tissue. At the microscopic level, we used a mass-spring model to describe the geometric structure and basic properties of onion epidermis tissue. The macroscopic domain was discretized using standard finite elements, in which the unknown material properties (the stress-strain relation) were computed using the microscopic model in small subdomains (the RVEs). To these RVEs, a macroscopic deformation was applied via appropriate boundary conditions, and from the equilibrium solution, the corresponding Cauchy stress was computed via a virial stress formula. The spatial elasticity tensor was estimated via forward differencing of the Truesdell rate of the Cauchy stress.

We have demonstrated via extensive numerical experiments that the resulting computational multi-scale method converges to the solution of the full microscopic solution, both for globally and locally adaptively refined meshes, and we have examined the influence of the size of the RVE (and the boundary conditions) on the efficiency and accuracy of the method. When comparing

the micro-macro approach to a full microscopic simulation, we observed a significant speed-up, even when the separation in spatial scales is not very large.

The microscopic model that was used in this work only accounts for the elastic part of the deformation. To explain *why* plant tissue exhibits visco-elasto-plastic behavior, we will, in future work, extend the microscopic modeling approach to take into account the viscosity of the cell fluid (instead of just modeling the cell fluid as a volume constraint), as well as the other hypotheses that were described in the introduction. While, in the present paper, we have restricted ourselves to a finite element formulation of *elastic* deformation at the macroscopic level as well, we emphasize that the proposed multi-scale approach can also be gradually refined to deal with the more general case of visco-elasto-plastic deformation. In Kouznetsova *et al* [24, 25], the transient deformation behavior of a wide range of heterogeneous materials (metal alloy systems, polymer blends, polycrystalline materials and composites) has been simulated. In such cases, the deformed RVE at the previous time-step should be used to apply new deformations and deformation velocities for the next time increment. Thus the state of the RVE at every quadrature point has to be kept in memory.

A second issue that requires further investigation is the size of the RVE when dealing with complex cellular structures. When studying more complex plants (e.g. apple or pear), the tissue can no longer be modeled as a periodic micro-structure, since the presence of cells of different sizes, as well as inter-cellular spaces need to be accounted for. This affects the size of the RVE, which will be necessary be larger to get a statistically representative sample of the underlying tissue [35]. Moreover, averaging over multiple runs with different initializations of the micro-structure might be necessary to reduce the statistical error. Finally, when dealing with larger RVEs, periodic boundary conditions might no longer be suitable.

## Acknowledgments

The authors would like to thank Varvara Kouznetsova for interesting and helpful discussions. This paper presents research results of the Belgian Network DYSCO (Dynamical Systems, Control, and Optimization), funded by the Interuniversity Attraction Poles Programme, initiated by the Belgian State, Science Policy Office. The scientific responsibility rests with its authors. This research was supported by the Fund for Scientific Research – Flanders through Research Project (3E060094). GS is a Postdoctoral Fellow of the Research Foundation - Flanders (FWO).

## A Appendix

In this appendix, the equality  $\mathbf{F}_M = \bar{\mathbf{F}}_\mu$  is proven for the case of the shifted periodic boundary conditions. Starting from the definition of the volume averaged microscopic deformation gradient, applying Green's identity and the fact that  $\mathbf{F}_\mu = \nabla_0 \mathbf{x}$  we get

$$\bar{\mathbf{F}}_\mu = \frac{1}{V^0} \int_{V^0} \mathbf{F}_\mu dV_0 = \frac{1}{V^0} \int_{\Gamma^0} \mathbf{x} \otimes \mathbf{N} d\Gamma^0$$

with  $\mathbf{N}$  the outward pointing normal vector on the boundary  $\Gamma^0$  of the volume  $V^0$ . The volume  $V^0$  refers to the volume of one undeformed cell. Let  $\Gamma^{1-3}$  be the piece of cell boundary connecting nodes 1, 2 and 3. The edges  $\Gamma^{3-5}$ ,  $\Gamma^{5-10}$ ,  $\Gamma^{10-8}$ ,  $\Gamma^{8-6}$  and  $\Gamma^{6-1}$  are defined in a similar way. Since  $\Gamma^0 = \Gamma^{1-3} + \Gamma^{3-5} + \Gamma^{5-10} + \Gamma^{10-8} + \Gamma^{8-6} + \Gamma^{6-1}$  the integral can be split as a sum over the different parts of the boundary. The coordinates of the deformed points on the boundary  $\Gamma^{1-3}$  are denoted as  $\mathbf{x}^{1-3}$  and  $\mathbf{x}^3$ ,  $\mathbf{x}^6$  and  $\mathbf{x}^{10}$  are the coordinates of the fixed nodes 3, 6 and 10. Using the periodicity of the boundary gives

$$\begin{aligned} \int_{\Gamma^{1-3}} \mathbf{x}^{1-3} \otimes \mathbf{N}^{1-3} d\Gamma^{1-3} &= - \int_{\Gamma^{10-8}} (\mathbf{x}^{10-8} + \mathbf{x}^3 - \mathbf{x}^{10}) \otimes \mathbf{N}^{10-8} d\Gamma^{10-8} \\ &= - \int_{\Gamma^{10-8}} (\mathbf{x}^{10-8} + \mathbf{F}_M \mathbf{X}^3 - \mathbf{F}_M \mathbf{X}^{10}) \otimes \mathbf{N}^{10-8} d\Gamma^{10-8} \end{aligned}$$

were  $\mathbf{N}^{1-3} = -\mathbf{N}^{10-8}$  was used. The same can be done for the integrals over the edges  $\Gamma^{3-5}$  and  $\Gamma^{5-10}$ . Summing the six integrals and simplifying leads to

$$\bar{\mathbf{F}}_\mu = \frac{\mathbf{F}_M}{V^0} \left( \int_{\Gamma^{10-8}} (\mathbf{X}^{10} - \mathbf{X}^3) \otimes \mathbf{N}^{10-8} d\Gamma^{10-8} + \int_{\Gamma^{8-6}} (\mathbf{X}^6 - \mathbf{X}^3) \otimes \mathbf{N}^{8-6} d\Gamma^{8-6} + \int_{\Gamma^{6-1}} (\mathbf{X}^6 - \mathbf{X}^{10}) \otimes \mathbf{N}^{6-1} d\Gamma^{6-1} \right). \quad (22)$$

The RVE is rectangular with width  $w$  and height  $h$ , so that  $V_0 = hw$ . Using this we finally get

$$\begin{aligned} \bar{\mathbf{F}}_\mu &= \frac{\mathbf{F}_M}{V^0} \left( \int_{\Gamma^{10-8}} \begin{bmatrix} 0 & -\frac{w}{2} \\ 0 & h \end{bmatrix} d\Gamma^{10-8} + \int_{\Gamma^{8-6}} \begin{bmatrix} 0 & \frac{w}{2} \\ 0 & h \end{bmatrix} d\Gamma^{8-6} + \int_{\Gamma^{6-1}} \begin{bmatrix} w & 0 \\ 0 & 0 \end{bmatrix} d\Gamma^{6-1} \right) \\ &= \frac{\mathbf{F}_M}{V^0} \left( \begin{bmatrix} 0 & -\frac{w^2}{4} \\ 0 & \frac{hw}{2} \end{bmatrix} + \begin{bmatrix} 0 & \frac{w^2}{4} \\ 0 & \frac{hw}{2} \end{bmatrix} + \begin{bmatrix} wh & 0 \\ 0 & 0 \end{bmatrix} \right) = \frac{\mathbf{F}_M}{V^0} \begin{bmatrix} hw & 0 \\ 0 & hw \end{bmatrix} \\ &= \mathbf{F}_M \end{aligned}$$

which concludes the proof.

## References

- [1] W. Bangerth, R. Hartmann, and G. Kanschat. deal.II — a general-purpose object-oriented finite element library. *ACM Transactions on Mathematical Software*, 33(4):24, August 2007. Article 24, 27 pages.
- [2] A. Bensoussan, J. L. Lions, and G. Papanicolaou. *Asymptotic analysis for periodic structures*, volume 5. North Holland Publishing Co, 1978.
- [3] J. Blewett, K. Burrows, and C. Thomas. A micromanipulation method to measure the mechanical properties of single tomato suspension cells. *Biotechnology Letters*, 22(23):1877–1883, 2000.
- [4] J. Bonet and R. D. Wood. *Nonlinear continuum mechanics for finite element analysis*. Cambridge University Press, 1997.
- [5] J. R. Brockenbrough, S. Suresh, and H. A. Wienecke. Deformation of metal-matrix composites with continuous fibers: geometrical effects of fiber distribution and shape. *Acta Metallurgica et Materialia*, 39(5):735–752, 1991.
- [6] P. N. Brown and Y. Saad. Hybrid Krylov methods for nonlinear systems of equations. *SIAM Journal on Scientific and Statistical Computing*, 11(3):450–481, 1990.
- [7] D. M. Bruce. Mathematical modelling of the cellular mechanics of plants. *Philosophical Transactions of the Royal Society B: Biological Sciences*, 358:1437–1444, 2003.
- [8] W. Chen and J. Fish. A mathematical homogenization perspective of virial stress. *International Journal for Numerical Methods in Engineering*, 67:189–207, 2006.
- [9] J. Cormier, J. M. Rickman, and T. J. Delph. Stress calculation in atomistic simulations of perfect and imperfect solids. *Journal of Applied Physics*, 89:99–104, 2001.
- [10] P. A. Cundall and O. D. L. Strack. A discrete numerical model for granular assemblies. *Geotechnique*, 29(1):47–65, 1979.
- [11] J. D. Eshelby. The determination of the elastic field of an ellipsoidal inclusion, and related problems. *Proceedings of the Royal Society of London. Series A, Mathematical and Physical Sciences*, 241:376–396, 1957.

- [12] F. Feyel and J. L. Chaboche. FE2 multiscale approach for modelling the elastoviscoplastic behaviour of long fibre SiC/Ti composite materials. *Computer Methods in Applied Mechanics and Engineering*, 183(3):309–330, 2000.
- [13] L. J. Gibson and M. F. Ashby. *Cellular Solids: Structure and Properties*. Cambridge University Press, 1997.
- [14] A. Gloria. An analytical framework for the numerical homogenization of monotone elliptic operators and quasiconvex energies. *Multiscale Modeling and Simulation*, 3:996–1043, 2006.
- [15] Z. Hashin and S. Shtrikman. A variational approach to the theory of the elastic behavior of polycrystals. *Journal of the Mechanics and Physics of Solids*, 10:343–352, 1962.
- [16] D. G. Hepworth and D. M. Bruce. A method of calculating the mechanical properties of nanoscopic plant cell wall components from tissue properties. *Journal of Materials Science*, 35(23):5861–5865, 2000.
- [17] T. J. R. Hughes. Equivalence of finite elements for nearly incompressible elasticity. *Journal of Applied Mechanics*, 44:181–183, 1977.
- [18] T. J. R. Hughes, M. Cohen, and M. Haroun. Reduced and selective integration techniques in finite element analysis of plates. *Nuclear Engineering Design*, 45:203–222, 1978.
- [19] J. H. Irving and J. G. Kirkwood. The statistical mechanical theory of transport processes, IV. The equations of hydrodynamics. *Journal of Chemical Physics*, 18:817–829, 1950.
- [20] MC Jarvis. Intercellular separation forces generated by intracellular pressure. *Plant, Cell & Environment*, 21(12):1307–1310, 1998.
- [21] J. Keckes, I. Burgert, K. Fruhmann, M. Muller, K. Kolln, M. Hamilton, M. Burghammer, SV Roth, S. Stanzl-Tschegg, and P. Fratzl. Cell-wall recovery after irreversible deformation of wood. *Nat Mater*, 2(12):810–4, 2003.
- [22] C. T. Kelley. *Solving nonlinear equations with Newton’s method*. Fundamentals of Algorithms. SIAM, Philadelphia, 2003.
- [23] L. Köhler and H.C. Spatz. Micromechanics of plant tissues beyond the linear-elastic range. *Planta*, 215(1):33–40, 2002.
- [24] V. Kouznetsova, W. A. M. Brekelmans, and F. P. T. Baaijens. An approach to micro-macro modeling of heterogeneous materials. *Computational Mechanics*, 27:37–48, 2001.
- [25] V. Kouznetsova, M. G. D. Geers, and W. A. M. Brekelmans. Multi-scale constitutive modelling of heterogeneous materials with a gradient-enhanced computational homogenization scheme. *International Journal for Numerical Methods in Engineering*, 54:1235–1260, 2002.
- [26] V. Kouznetsova, M. G. D. Geers, and W. A. M. Brekelmans. Multi-scale second-order computational homogenization of multi-phase materials: a nested finite element solution strategy. *Computer Methods in Applied Mechanics and Engineering*, 193:5525–5550, 2004.
- [27] J. Loodts, E. Tijskens, C. Wei, E. Vanstreels, B. Nicolai, and H. Ramon. Micromechanics: Simulating the elastic behavior of onion epidermis tissue. *Journal of Texture Studies*, 37:16–34, February 2006.
- [28] R. Lu and V. M. Puri. Characterization of nonlinear creep behavior of two food products. *Journal of Rheology*, 35:1209, 1991.
- [29] T. J. Massart, R. H. J. Peerlings, and M. G. D. Geers. An enhanced multi-scale approach for masonry wall computations with localization of damage. *International journal for numerical methods in engineering*, 69(5):1022–1059, 2007.

- [30] C. Miehe. Numerical computation of algorithmic (consistent) tangent moduli in large-strain computational inelasticity. *Computer Methods in Applied Mechanics and Engineering*, 134:223–240, August 1996.
- [31] C. Miehe, J. Schroder, and J. Schotte. Computational homogenization analysis in finite plasticity simulation of texture development in polycrystalline materials. *Computer Methods in Applied Mechanics and Engineering*, 171(3-4):387–418, April 1999.
- [32] J. P. Mittal, N. N. Mohsenin, and M. G. Sharma. Rheological characterization of apple cortex. *Journal of Texture Studies*, 18(1):65–93, 1987.
- [33] T. Mori and K. Tanaka. Average stress in matrix and average elastic energy of materials with misfitting inclusions. *Acta Materialia*, 21(5):571–574, 1973.
- [34] S. Nemat-Nasser and M. Hori. *Micromechanics: Overall Properties of Heterogeneous Solids*. Elsevier, Amsterdam, 1993.
- [35] M. Ostoja-Starzewski. Material spatial randomness: From statistical to representative volume element. *Probabilistic Engineering Mechanics*, 21(2):112–132, 2006.
- [36] M. Pernice and H. F. Walker. NITSOL: A Newton Iterative Solver for Nonlinear Systems. *SIAM Journal on Scientific Computing*, 19(1):302–318, 1998.
- [37] Weiqing Ren. Seamless multiscale modeling of complex fluids using fiber bundle dynamics. *Communications in Mathematical Sciences*, 5(4):1027–1037, 2007.
- [38] PG Saffman and G. Taylor. The Penetration of a Fluid into a Porous Medium or Hele-Shaw Cell Containing a More Viscous Liquid. *Proceedings of the Royal Society of London. Series A, Mathematical and Physical Sciences (1934-1990)*, 245(1242):312–329, 1958.
- [39] J. C. Simo and T. J. R. Hughes. *Computational inelasticity*. Springer New York, 1998.
- [40] J. C. Simo and M. S. Rifai. A class of mixed assumed strain methods and the method of incompatible modes. *International Journal for Numerical Methods in Engineering*, 29(8):1595–1638, 1990.
- [41] R. J. M. Smit, W. A. M. Brekelmans, and H. E. H. Meijer. Prediction of the mechanical behavior of nonlinear heterogeneous systems by multi-level finite element modeling. *Computer Methods in Applied Mechanics and Engineering*, 155(1-2):181–192, 1998.
- [42] K.R. Spring. Routes and mechanisms of fluid transport by epithelia. *Annual Reviews in Physiology*, 60(1):105–119, 1998.
- [43] K. Terada, M. Hori, T. Kyoya, and N. Kikuchi. Simulation of the multi-scale convergence in computational homogenization approaches. *International Journal of Solids and Structures*, 37:2285–2311, April 2000.
- [44] O. van der Sluis, P. J. G. Schreurs, and H. E. H. Meijer. Effective properties of a viscoplastic constitutive model obtained by homogenisation. *Mechanics of Materials*, 31(11):743–759, 1999.
- [45] E. Vanstreels, M. C. Alamar, B. E. Verlinden, A. Enninghorst, J. K. A. Loodts, E. Tijskens, H. Ramon, and B. M. Nicolaï. Micromechanical behaviour of onion epidermal tissue. *Postharvest Biology and Technology*, 37(2):163–173, 2005.
- [46] B. Verleye, M. Klitz, R. Croce, D. Roose, S. Lomov, and I. Verpoest. Computation of permeability of textile reinforcements. *Proc. 9th Int. Conf. on Material Forming (ESAFORM-9)*, Glasgow, United Kingdom, pages 735–738, 2006.

- [47] C. Wei, P. M. Lintilhac, and J. J. Tanguay. An insight into cell elasticity and load-bearing ability. Measurement and theory. *Journal of Plant Physiology*, 126:1129–1138, 2001.
- [48] J.T. Woolley. Maintenance of air in intercellular spaces of plants. *Plant Physiology*, 72(4):989, 1983.
- [49] M. Zhou. A new look at the atomic level virial stress: on continuum-molecular system equivalence. *Proceedings: Mathematical, Physical & Engineering Sciences*, 459:2347–2392, 2003.
- [50] O. C. Zienkiewicz and R. L. Taylor. *The Finite Element Method for Solid and Structural Mechanics, Sixth Edition*. Butterworth-Heinemann, 2005.
- [51] O. C. Zienkiewicz and R. L. Taylor. *The Finite Element Method: Its Basis and Fundamentals, Sixth Edition*. Butterworth-Heinemann, 2005.